Hindawi
Shock and Vibration
Volume 2020, Article ID 8850079, 15 pages
https://doi.org/10.1155/2020/8850079

Research Article

High-Frequency Vibration Analysis and Optimization of Irregular Wear of Pantograph Carbon Strips

Chao Huang,[1] Anbin Wang,[1] Xiaohan Gu,[1] Xiaogang Gao,[1] Yu He,[1] Lang Liu,[1] and Feng Gao[2]

[1]*School of Urban Railway Transportation, Shanghai University of Engineering Science, Shanghai 201620, China*
[2]*School of Air Transport, Shanghai University of Engineering Science, Shanghai 201620, China*

Correspondence should be addressed to Anbin Wang; anbin.wang@sues.edu.cn

Received 22 May 2020; Revised 15 July 2020; Accepted 18 July 2020; Published 30 August 2020

Academic Editor: Marco Alfano

The irregular wear of carbon current collector pantograph strips increases the railway maintenance costs and introduces safety hazards in the railway operation. This paper presents a method for analyzing the irregular wear of carbon strips with numerical dynamic analyses and modal tests. The carbon strips were studied in laboratory tests, and an equivalent numerical model for the investigation of their irregular wear and performance improvement was established. The results from the computational simulations were evaluated based on the laboratory results, and the correlation between the high-frequency vibration and irregular wear of the carbon strips was studied. The irregular wear contour of the carbon strips coincides with the high-frequency mode shape according to the experimental and numerical results. Moreover, the dynamic design for carbon strips was optimized with the validated computational model. The results suggest that the optimized schemes effectively mitigate the irregular wear of carbon strips.

1. Introduction

Electric buses in metro railway systems suffer from the irregular wear of the pantograph strips. In general, a pantograph carbon strip with irregular wear has the following two features: (1) The vertical direction of the pantograph strip has one or more grooves of different depths. (2) The slant wear of the pantograph strip (i.e., its transverse thickness) is different. Wear can mainly be classified into mechanical wear and electrical wear [1–3]. Many researchers have shown that, for example, the contact normal load, current, and sliding speed have significant effects on the friction and wear between the carbon strip and contact line (the current has the greatest effect on the carbon strip) [4–6].

Nevertheless, with increasing train speed, dynamic parameters such as the up-and-down inertia force, gas dynamic component force, and train disturbance force generated by the pantograph movement have increasing influences on the contact state of the pantograph. For metro railway systems, when the train is moving at a high speed, the interaction between the rigid catenary and carbon strip, which leads to the high-frequency vibration of the carbon strip, indirectly causes or aggravates the irregular wear of the latter [7, 8]. Recent studies have shown the complex relationship between the vibration characteristics and wear of carbon strips. For example, Yang et al. studied the effect of vibrations on the friction and wear behavior of carbon wires and copper contact lines [9]. The results show that the contact loss due to the low-frequency vibrations of the strips is one of the main causes leading to arc discharge, which aggravates the wear of carbon strips and contact lines. Mei detected vibration of the slider during a metro rigid catenary sliding against a pantograph strip with DC [10]. The results indicate that arc ablation and vibration of the slider are two important factors to cause severe wears of the strip and wire. Zhang et al. combined finite-element model calculations and laboratory tests on pantograph carbon strips [11]. The experimental results show that the vibration frequency of the carbon strip has different effects on its friction coefficient and wear rate at different speeds. Moreover, Bucca et al. analyzed the electromechanical interaction between a carbon strip and copper contact line [12]. The researchers combined the

dynamic electromechanical and wear models for carbon strips to estimate the wear amount caused by the dynamic interaction between a carbon strip and contact line. Focusing on the wear problems that occur on the contact wire and the pantograph strip used in metro system, Wei et al. carried out the wear mechanism, wear analysis, wear calculation, and prediction [13]. The results illustrate that, in order to prevent the huge uneven wear profile on the pantograph strip, the contact wire with high stagger value should be located away from the acceleration zone to avoid high wear rate and long wear distance occurring on the small interval of pantograph strip in the same time. Zhou and Zhang analyzed the interaction between the carbon slide and catenary with the finite-element method [14]. According to the results, frequency components of 40–100 Hz have a great effect on the dynamic contact force and acceleration of the carbon strip. Shi et al. conducted fault diagnosis based on carbon strip vibration signal and verified the feasibility and effectiveness of pantograph carbon strip vibration signal fault diagnosis by combining modern time-frequency analysis algorithm and the information entropy [15].

The high-frequency vibrations (over 100 Hz) of the bow net and friction and wear of carbon strips have not been sufficiently investigated. Nevertheless, studying and suppressing the high-frequency vibrations of carbon strips to ensure the reasonable movement and matching between pantographs and catenaries are crucial for safe operation.

In this study, a rigid catenary, nonlinear single-degree-of-freedom pantograph, and bow-net coupling models were established. The carbon strips were investigated in vertical and transverse vibration modal tests, and the pantograph model was evaluated. In addition, the vibration mode shapes were compared with the irregular wear patterns of the carbon strips to determine the high-frequency vibration range related to the irregular wear. Finally, the multiparameter method was used to optimize the design of the carbon strip structure to mitigate irregular wear. The high-frequency (over 100 Hz) vibration mode was studied to analyze the irregular wear profile of the carbon strip. According to the results, this study provides a feasible solution for the analysis of irregular wear of pantograph carbon strips.

2. Numerical Model

2.1. Rigid Catenary Model. In general, a rigid catenary comprises several successive sections. One section mainly consists of aluminum profiles that are connected by flanges. The lower part of the aluminum profile is a fixed contact wire, and the upper part is fixed to the supports. In this study, a two-dimensional model [16] with train movement in the x-axis direction was considered; the pantograph and rigid catenary interact in the y-axis direction (Figure 1). Table 1 lists the catenary parameters for the numerical model.

Thus, the differential equation of motion of the rigid catenary can be expressed as follows:

$$\mathbf{M}\ddot{v} + \mathbf{C}\dot{v} + \mathbf{K}\mathbf{v} = \mathbf{f}, \tag{1}$$

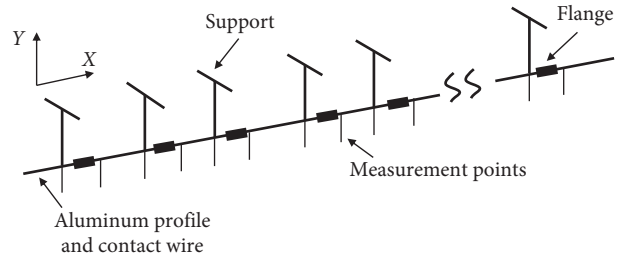

Figure 1: Finite-element model of rigid catenary.

where **M**, **C**, and **K** are the mass, damping, and stiffness matrices of the catenary, respectively; **f** is the load vector of the catenary node; and $\ddot{v}$, $\dot{v}$, and **v** are the catenary node acceleration, velocity, and node displacement vectors, respectively.

2.2. Pantograph Model. The pantograph is installed on top of the train to receive current from the catenary. Pantographs can mainly be classified into two types: single- and two-arm pantographs. Owing to the structural design limit and excessive aerodynamic noise during operation, the two-arm structure has been gradually replaced with the single-arm structure. The system generally includes the following components: bottom frame, lower arm, upper arm, connecting rod, balance rod, bow head bracket, carbon strip, bow angle, and other mechanical parts. To simplify the computation, the pantograph is considered to move vertically (Figure 2). Table 2 lists the parameters of the pantograph numerical model.

As depicted in Figure 2, A, B, C, and E are the hinge points of the lower arm and brace. The dashed line represents the auxiliary line of the calculation process, and a, b, c, and d represent each arm. Moreover, d_1 and d_2 are the two coordinates of the hinge point E; L is the bow head position; G is the vertex of the upper arm; H is the center of the upper arm; and d_3 is the distance to the hinge point B. In addition, F_C is the contact force between the bow head and catenary, and F_L is the interaction force between the bow head and pantograph system. The angle between the brace and negative x-axis direction in generalized coordinates is θ; the angle between the lower arm and negative x-axis direction is ϕ_1; the angle between the upper arm and positive x-axis direction is ϕ_2; the angle between BC and the brace is ϕ_3. According to (2), ϕ_1, ϕ_2, y_G, and (x_H, y_H) can be expressed as functions of θ:

$$\phi_3 = \arccos\left(\frac{a^2 + f^2 - b^2}{2af}\right), \tag{2}$$

$$f_1 = \operatorname{arctg}\left[\frac{f\sin(f_3 + \theta) - d_1}{f\cos(f_3 + \theta) + d_2}\right], \tag{3}$$

$$\phi_2 = \arccos\left(\frac{d^2 + c^2 - e^2}{2\quad dc}\right) - \phi_1, \tag{4}$$

$$y_G = f\sin(f_1 + \theta) + c\sin f_1, \tag{5}$$

Table 1: Simulation model parameters for rigid catenary.

Component	Parameter	Value	Unit
General	Number of spans	20	
	Span length	10	m
Aluminum profile and contact wire	Section area	25	cm^2
	Inertia flexural property	4.1×10^{-6}	m^4
	Density	2900	kg/m^3
	Young modulus	6.9×10^{10}	N/m^2
Support	Support stiffness	400	kN/m
Flange	Weight	3	kg
	Moment of inertia	2.4×10^{-3}	$kg \cdot m^2$

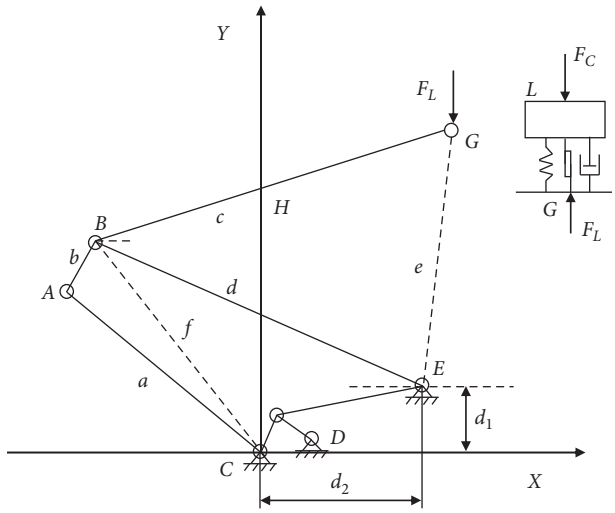

Figure 2: Simplified vertical-structure simulation model of pantograph.

Table 2: Simulation model parameters for pantograph.

Component	Material	Elastic modulus (GPa)	Poisson's ratio	Density ($kg \cdot m^{-3}$)	Cross-sectional area (mm^2)
Bow head bracket	Aluminum alloy	72	0.33	2800	300
Bow head strip	Carbon	12.4	0.35	2000	300
Upper frame	Steel	210	0.3	7850	600
Balance bar	Steel	210	0.3	7850	7800
Putter	Steel	210	0.3	7850	1250

$$x_H = f\cos(f_1 + \theta) - d_3\cos f_1;$$
$$y_H = f\sin(f_1 + \theta) + d_3\sin f_1. \quad (6)$$

Equations (3)–(6) can be obtained as follows:

$$k_1 = \frac{\delta\phi_1}{\delta\theta}; k_2 = \frac{\delta\phi_2}{\delta\theta}; k_3 = \frac{\delta y_G}{\delta\theta}; k_4 = \frac{\delta x_H}{\delta\theta}; k_5 = \frac{\delta y_H}{\delta\theta}. \quad (7)$$

The parameters w_a, w_c, and w_d are the angular velocities of the brace, upper arm, and lower arm, respectively; v_{yG} is the vertical velocity; and v_{xH} and v_{yH} represent the lateral and vertical velocities of point G, respectively:

$$w_a = \frac{d\theta}{dt}; w_c = k_2 w_a; w_d = k_1 w_a,$$
$$v_{y_G} = k_3 w_a; v_{x_H} = k_4 w_a; v_{y_H} = k_5 w_a. \quad (8)$$

Equation (9) can be obtained from the second-order Lagrangian equation:

$$\frac{d}{dt}\left(\frac{\partial T}{\partial \dot{q}_j}\right) - \frac{\partial T}{\partial q_j} + \frac{\partial V'}{\partial q_j} = Q'_j, \quad (9)$$

where q_j represents the generalized coordinates, T the kinetic energy, V' the potential energy, and $Q\prime j$ the generalized force of the system. According to the d'Alembert–Lagrange principle for generalized coordinates, the frame kinetic energy and potential energy in the pantograph system can be expressed as follows:

$$T = \frac{1}{2}J_a w_a^2 + \frac{1}{2}J_d w_d^2 + \frac{1}{2}J_c w_c^2 + \frac{1}{2}m_c\left(v_{x_H}{}^2 + v_{y_H}{}^2\right) \quad (10)$$

$$V\prime = m_a g a\sin\theta + m_d g d\sin\phi + m_c g c\sin\phi_2, \quad (11)$$

respectively, where J is the rotational modulus around the center of mass and m is the quality of the arm. Consequently,

the elemental work done by the main force can be expressed as follows:

$$Q_j'\delta\theta = \left(-F_L k_3 - C\frac{\mathrm{d}s}{\mathrm{d}t}\cdot\frac{\delta s}{\delta\theta} + M_x\right)\delta\theta, \tag{12}$$

where C is the damping number of the damping device and $C(\mathrm{d}s/\mathrm{d}t)$ is the damping force.

Based on the presented theory, the motion differential equation of the pantograph head is written as follows:

$$\mathrm{M_L}\ddot{y}_\mathrm{L} + \mathbf{C_L}\left(\dot{y}_\mathrm{L} - \dot{y}_\mathrm{G}\right) + \mathbf{K_L}\left(\mathbf{y_L} - \mathbf{y_G} - \mathbf{y_k}\right) + \mathbf{M_L g} = \mathbf{F_C}, \tag{13}$$

where $\mathbf{M_L}$ is the pantograph head mass matrix, $\mathbf{C_L}$ is the pantograph head damping matrix, $\mathbf{K_L}$ is the pantograph head stiffness matrix, $\ddot{y}_\mathbf{L}$ is the pantograph head node acceleration vector, $\dot{y}_\mathbf{L}$ and $\dot{y}_\mathbf{G}$ are the pantograph head node velocity vectors, $\mathbf{y_L}$ and $\mathbf{y_G}$ are the displacement vectors of the pantograph head node, $\mathbf{y_k}$ is the original length vector of the equivalent spring of the pantograph head, and $\mathbf{F_C}$ is the node load vector of the pantograph head.

2.3. Bow-Net Coupling Model. Based on [17], a contact element was placed between the contact wire and pantograph strip. When the pantograph strip slid along the contact wire, it was checked whether the contact wire node and pantograph strip node penetrated each other in the contact area; if not, the gap between the contact wire and pantograph strip was greater than zero; thus, the dynamic contact force was zero; if they penetrated each other, a greater interface contact force was introduced between the contact wire and pantograph carbon strip; the force was directly proportional to the penetration depth and interface stiffness. Therefore, the motion differential equation of the bow-net coupling system can be expressed as follows:

$$\mathbf{M_p}\ddot{u} + \mathbf{C_p}\dot{u} + \mathbf{K_p u} = \mathbf{F_p}, \tag{14}$$

where $\mathbf{M_p}$, $\mathbf{C_p}$, and $\mathbf{K_p}$ are the mass, damping, and stiffness matrices of the bow-net system, respectively; $\ddot{u}$, $\dot{u}$, and $\mathbf{u}$ are the acceleration, velocity, and displacement vectors of the bow-net system nodes, respectively. In addition, $\mathbf{F_p}$ is the node load vector of the bow-net system.

3. Analysis of Vibration Characteristics

3.1. Numerical Modal Analysis. By considering the vibration characteristics of the pantograph strip, the modal analysis was conducted based on the numerical model presented in Section 2. The geometry of the model was built in SolidWorks and analyzed with the commercial software ABAQUS. The calculation parameters of the pantograph strip are listed in Table 2, and the identified modal frequencies and mode shapes are presented in Figure 3.

3.2. Experimental Modal Analysis. The vibrations in the vertical and transverse directions are most relevant to pantograph strips [18, 19]; they affect the dynamic contact pressure of the carbon strip and contact wire. An abnormal contact pressure causes irregular wear on the carbon strip, which affects the contact pressure [20]. In addition, transverse vibrations affect the relative dynamic sliding process of the carbon strip and contact wire. With increasing sliding speed, the cracks and depth in the carbon strip increase and lead to eccentric wear [21, 22]. In this study, an experimental modal analysis was conducted to study the vertical and transverse vibrations of the carbon strip.

A real carbon strip was selected for the experimental modal analysis, and the modal parameters of the carbon strip were identified in a frequency domain analysis. The experiment was conducted through multi-input multi-output channels [23]. To obtain as much modal information as possible, 13 excitation/measuring points were chosen and numbered (Figure 4). These 13 measuring points are equally spaced on the surface of the carbon strip; both strip ends have much lower stiffness values than the carbon strip low-order modal stiffness of rubber rope hanging fixed as free boundary conditions and select vibration picking point at 4 and 9 positions. Each set of tests is excised and sampled several times to eliminate errors in the frequency response function and background noise in the measured data. Figure 5 presents the flowchart of the experimental procedure.

3.3. Results and Validation. According to the correlation curve of the excitations and responses, the coherence coefficients of the vertical and transverse modal frequencies are close to 1.0 in the 0–1000 Hz frequency band. Thus, the measured data of the experiment are effective, the external noise is low, and the vibration characteristics of the carbon strip can reliably be reflected. Figure 6 summarizes the results of the frequency response functions of the first six vertical and transverse modes. The subfigures show the attenuation and amplification of the vibration frequency when the pulse is excited; the peak values of the curve represent the modal frequencies [24]. The frequency responses from the different measuring points and modal frequencies are consistent. By comparing Figures 6(a) and 6(b), it can be seen that the response peaks of the third, fourth, and fifth transverse modes are evidently higher, whereas the response peaks of the first and sixth modes are lower than those of the vertical modes. According to Figure 7, the modal frequencies of the first six vertical modes increase linearly. By contrast, the modal frequencies of the first six transverse modes increase nonlinearly. Hence, the vertical modes can be more easily controlled in the design optimization of carbon strips to avoid the resonance frequency of the carbon strip and catenary.

Figure 8 presents the vertical and transverse mode shapes of the carbon strip. According to Figure 8(a), the mode shapes of the first, third, and fifth modes have great influences on the vertical vibration of the central area of the carbon strip. Figure 8(b) shows the corresponding characteristics of the first, fourth, and sixth mode shapes. In Table 3, the transverse modal frequencies of all modes are greater than the vertical modal frequencies, and the damping ratio of the transverse modes is smaller than that of the vertical modes. Thus, the resonance frequency of the carbon

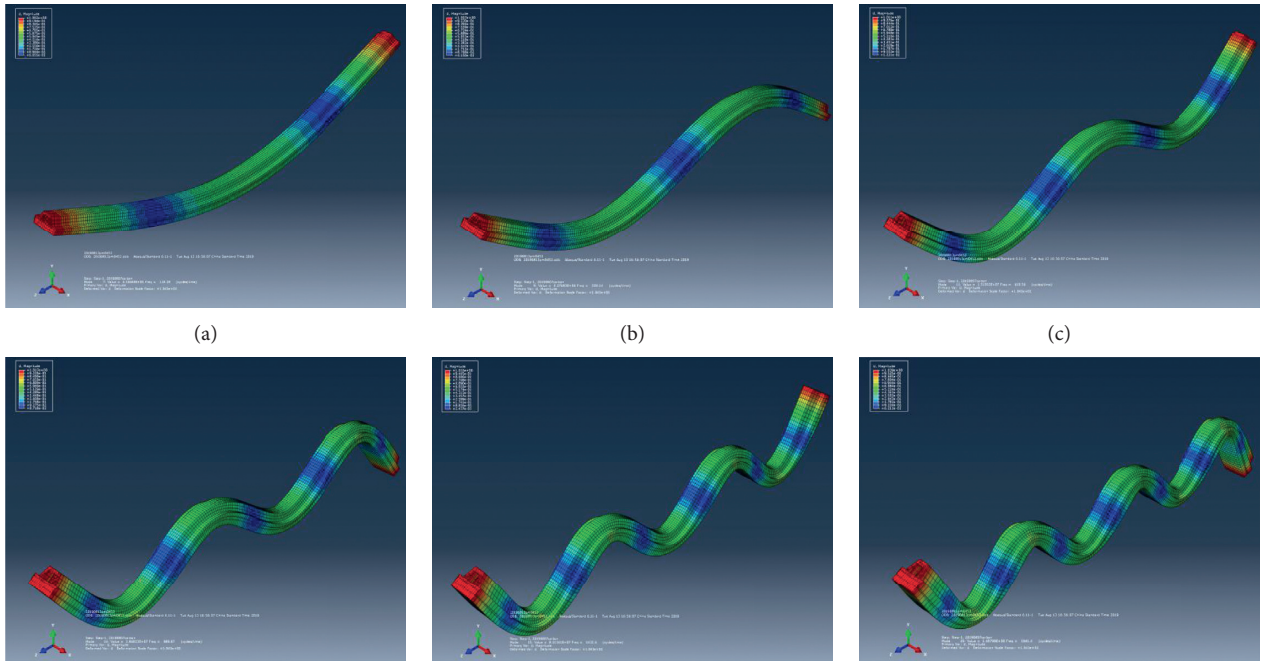

Figure 3: Mode shapes and modal frequencies of the first six vertical modes. (a) Mode 1,65.86 Hz. (b) Mode 2,139.81 Hz. (c) Mode 3,241.57 Hz. (d) Mode 4,389.10 Hz. (e) Mode 5,588.94 Hz. (f) Mode 6,810.66 Hz.

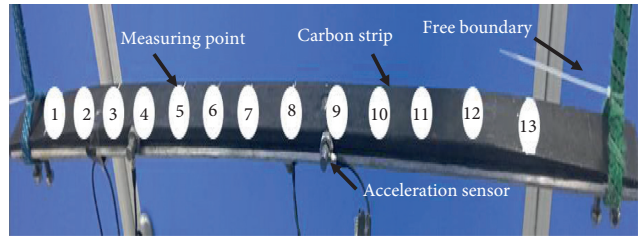

Figure 4: Arrangement of measuring points and acceleration sensors on the carbon strip.

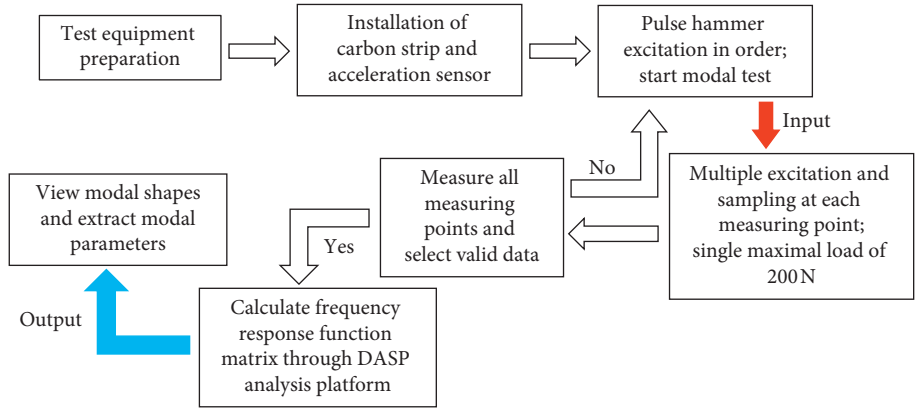

Figure 5: Modal test flow of carbon strip.

strip is different in different directions. Based on the definition of the damping ratio, it can be concluded that the vertical stiffness of the carbon strip is less than the transverse stiffness, which also indicates that the bending degree of the vertical mode shapes is more evident. Although the aerodynamics, electric locomotive excitation signal, and flow

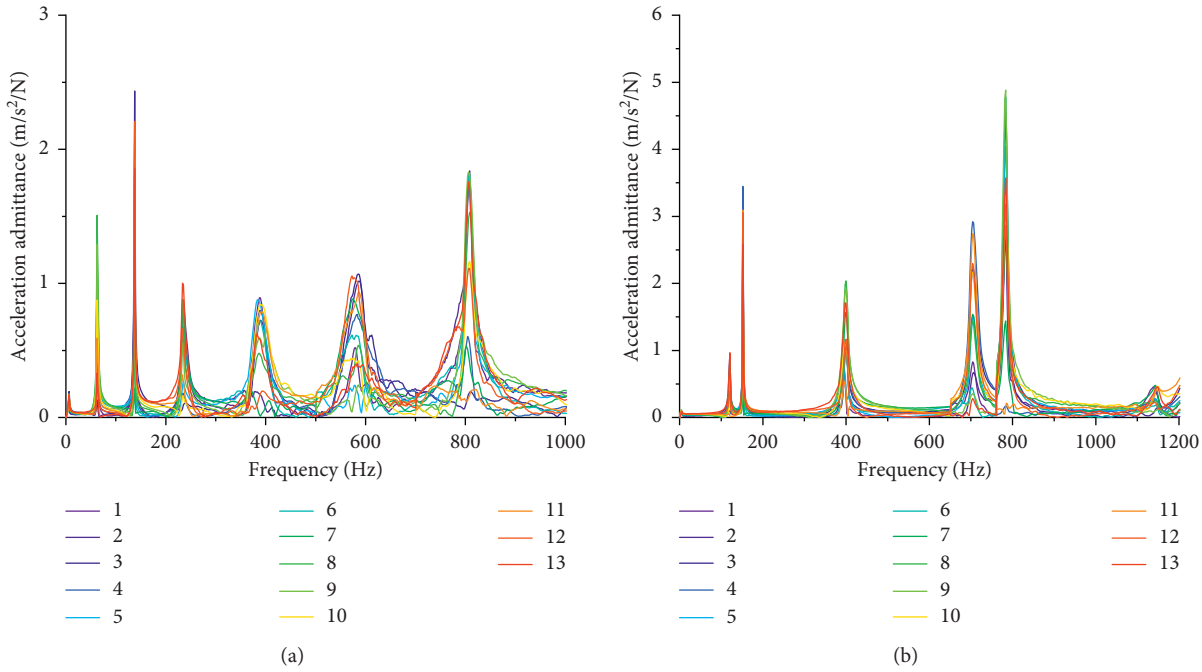

Figure 6: Frequency response functions of modal tests on carbon strip: (a) vertical and (b) transverse modal frequencies.

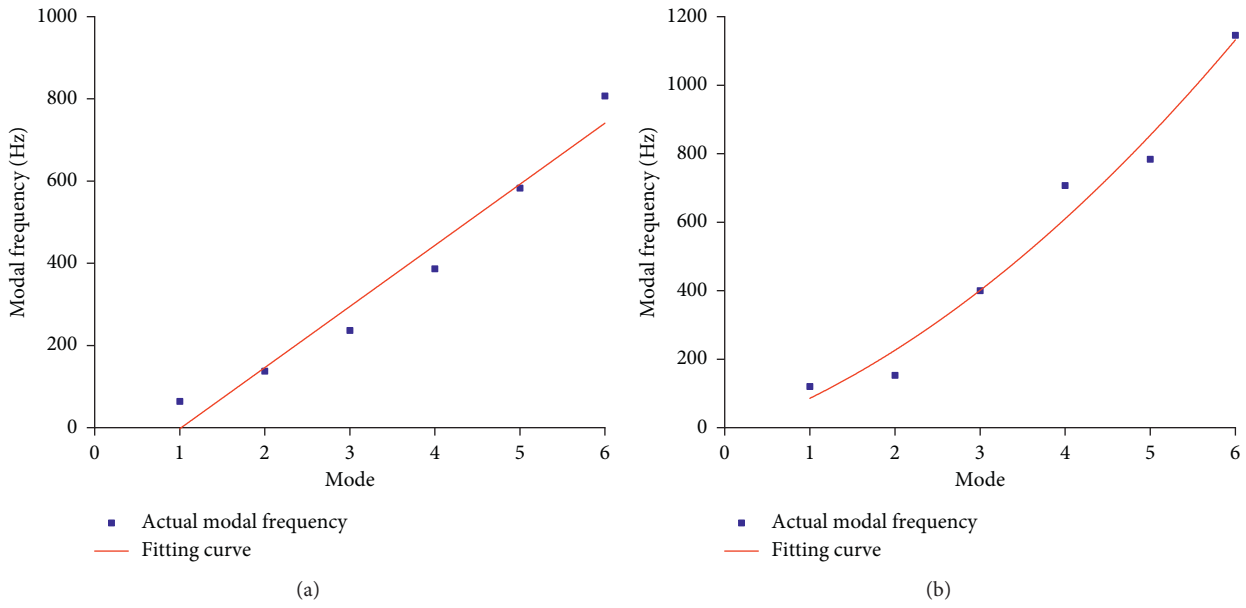

Figure 7: Modal frequency: (a) vertical and (b) transverse.

conditions were not considered in the modal analysis, the identified modal parameters accurately reflect the vibration characteristics of the carbon strip.

Table 4 compares the first six vertical modal frequencies of the laboratory test results with the simulation results. The maximal difference is 5.0 Hz, which corresponds to 3.4%. By comparing Figures 3 and 8(a), it can be seen that the bending distributions of the vertical mode shapes of all modes are consistent. These two results confirm each other.

4. Analysis of Irregular Wear

4.1. Carbon Strip Vibration Characteristics. The formation mechanism of irregular wear was mainly predicted based on the kinetic characteristics of the carbon strip and then simulated with the numerical method. Figure 9 presents the vertical profiles of the carbon strip before and after wear. Figure 9(b) shows the ideal wear profile: an approximately arc-shaped groove with symmetry at the center has been

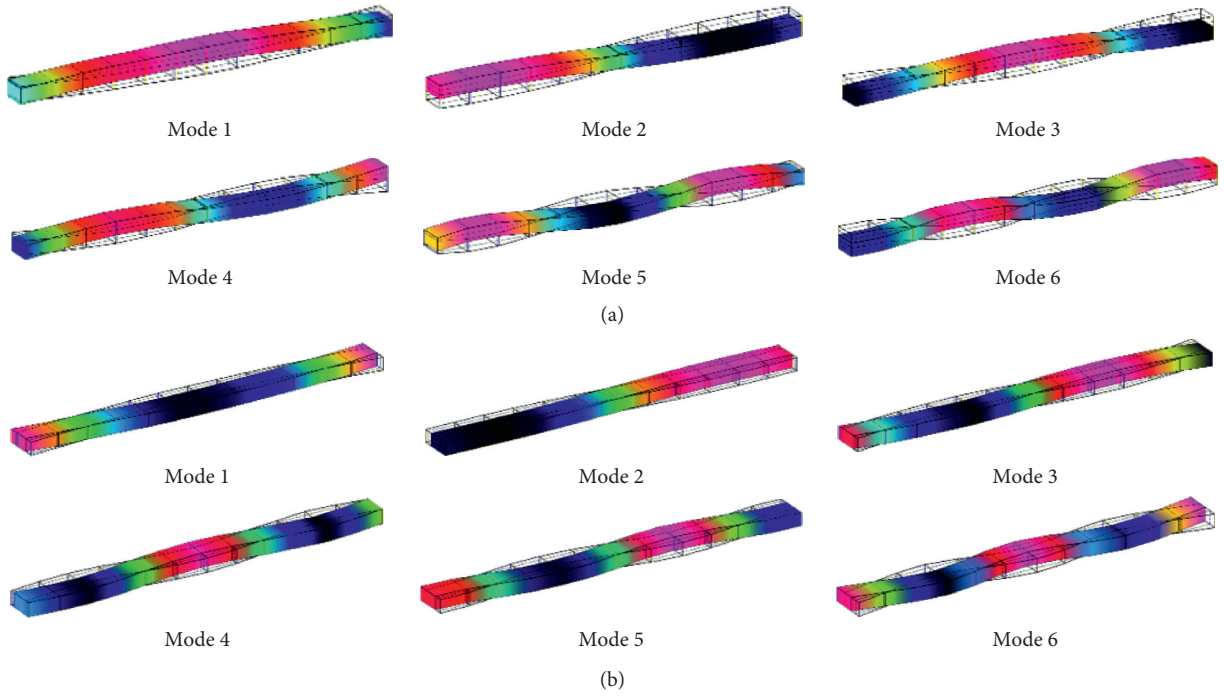

Figure 8: Test modal shapes of carbon strip: (a) vertical and (b) transverse.

Table 3: Modal parameters of vertical and transverse modes.

Mode	Frequency (Hz)/vertical	Damping ratio (%)/vertical	Frequency (Hz)/transverse	Damping ratio (%)/transverse
First	63.7	1.426	120.2	1.127
Second	137.5	0.532	152.6	0.332
Third	236.5	0.782	399.9	0.519
Fourth	386.7	1.652	706.8	1.074
Fifth	582.9	1.571	783.5	1.253
Sixth	807.3	0.580	1145.5	0.462

Table 4: Comparison of experimental and simulated vertical modal frequencies.

Mode	Simulation (Hz)	Laboratory test (Hz)	Discrepancy (%)
First	65.9	63.7	3.4
Second	139.8	137.5	1.7
Third	241.6	236.5	2.1
Fourth	389.1	386.7	0.6
Fifth	588.9	582.9	1.0
Sixth	810.7	807.3	0.4

formed in the vertical direction of the carbon strip. The actual carbon strip is presented in Figure 9(c); the red circle indicates the area of irregular wear. There are two approximately U-shaped grooves with shallow depth near the strip center and greater depths near the two strip ends. The profile is characterized by typical irregular wear, which comprises two grooves in the carbon strip. Owing to the different irregular wear profile depths, the typical two and three grooves were the main study objects.

4.2. Vertical Vibrations. The interaction and contact between the carbon strip in service and catenary generate an unsteady dynamic force F in the vertical direction, as depicted in Figure 10(a). Owing to the aerodynamic force and dynamic force F, the dynamic lifting amount of the catenary changes significantly; consequently, a dynamic contact pressure F_c is generated between the carbon strip and catenary:

$$F_c = K(y_L - y_1), \tag{15}$$

where y_L and y_1 represent the simultaneous displacements of the contact wire and carbon strip, respectively. When the carbon strip resonates with or encounters a "hard spot" in the catenary, the contact pressure decreases rapidly. In addition, the offline phenomenon occurs when the contact state is poor, and the carbon strip affected by the external force collides with the catenary. This unsteady process comprises contact–offline–collision–contact stages. The resulting fluctuating contact pressure and the external environment (e.g., the dynamic force of the air during train operation) cause the carbon strip to vibrate. In particular,

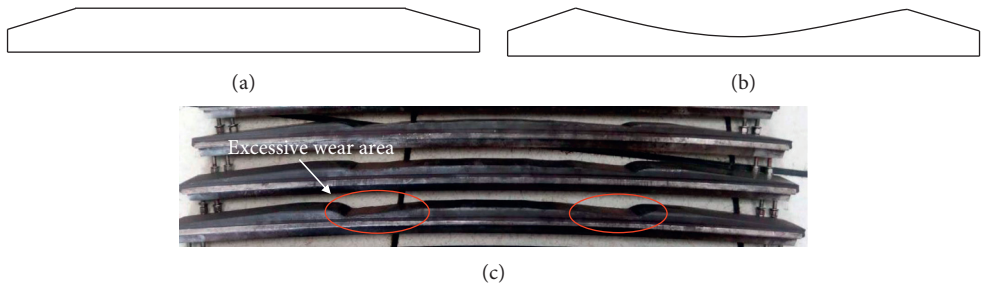

Figure 9: Comparison of carbon strip wear traces. (a) New carbon strip. (b) Carbon strip after abrasion (ideal case). (c) Carbon strip after abrasion (reality).

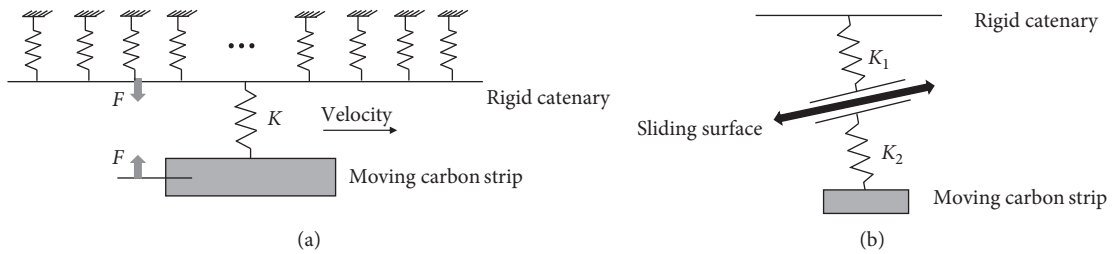

Figure 10: Interaction between carbon strip and catenary. (a) Vertical model. (b) Transverse model.

the high amplitude of the modal vibration affects the contact pressure. When the contact pressure increases, the friction between the carbon strip and catenary increases, which increases the mechanical wear. Simultaneously, the unsteady contact pressure, particularly in the contact–offline–collision–contact state, will cause different degrees of wear along the carbon strip. As a result, the dynamic lifting amount of the catenary introduces mechanical friction wear and arc wear.

4.3. Transverse Vibration. In addition to the vertical vibrations, which change the friction force and contact state caused by friction wear, the transverse and vertical sliding of the carbon strip and catenary is inevitable owing to the sliding and swinging movements during operation. At constant vehicle speed, the transverse vibration and vertical component of the carbon strip cause contact pressure fluctuations and transverse alternating sliding [25]. Figure 10(b) illustrates the transverse interaction between the carbon strip and catenary. It aggravates the wear caused by the vertical vibrations and expands the wear range in the transverse direction. Simultaneously, with increasing vehicle speed, the relative sliding speed between the carbon strip and catenary increases, which increases the frictional heat generated during mechanical wear. In addition, owing to the transverse vibration, the edges and corners of the carbon strip collide with the catenary; subsequently, the side of the carbon strip scratches off [26].

4.4. Analysis and Evaluation. By comparing the vertical mode shapes in Figure 8(a) with the typical two-groove profile in Figure 9(c), it can be seen that the third mode shape is consistent with the two-groove depth profile. The red dashed curve in Figure 11 represents the mode shape curves. As shown in Figure 11(a), the shape curve of the third mode and depth profile of the two grooves fit well. Figure 11(b) presents the vertical fifth mode shape curve and depth profile of the typical three grooves. Evidently, the curve trend is consistent with the profile. According to Table 3, the vertical third and fifth modal frequencies of the carbon strip are 236.5 and 582.9 Hz, respectively. Therefore, it is assumed that the high-frequency vibration of the carbon strip is correlated with the irregular wear, and 236.5 and 582.9 Hz are the high-frequency vibration frequencies that further aggravate its wear.

Limited by space, the mechanism of two grooves and high-frequency vibration is mainly validated. Based on the numerical model in Section 2, the catenary was set such that it balanced its own gravity and initial tension while considering the actual running speed of subways. The pantograph strip moved along the catenary at 60 km/h and the sampling and filtering frequencies were 600 and 300 Hz, respectively. The resulting dynamic contact force and spectrum of the contact force between the carbon strip and catenary are presented in Figure 12; the vertical vibration acceleration and spectrum of the carbon strip are shown in Figure 13.

As shown in Figure 12, the carbon strip is offline in three sampling points when the pantograph runs at 60 km/h. The contact force fluctuates around 110 N at the other stages, thereby indicating that the contact force changes instantaneously owing to the impact force of the great amplitude at the offline stage. Moreover, Figure 12(b) presents the spectrum of the contact pressure of the carbon strip. The contribution at approximately 20 Hz is the greatest, followed

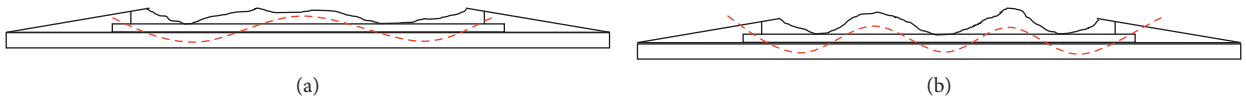

(a) (b)

Figure 11: Comparison of irregular abrasion profiles and vertical modal shapes.

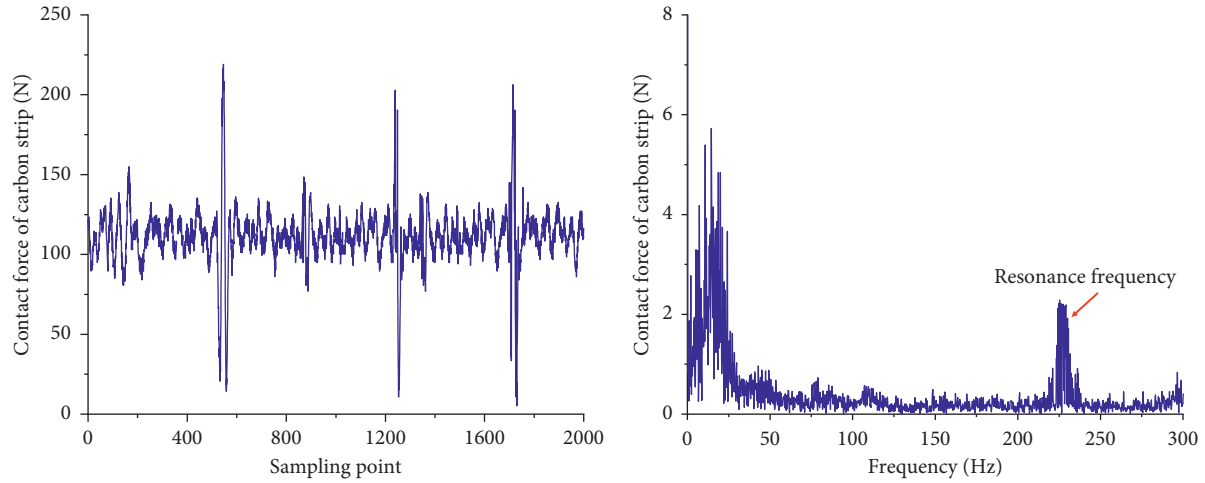

(a) (b)

Figure 12: Time-domain diagram and spectrum of contact force between carbon strip and catenary.

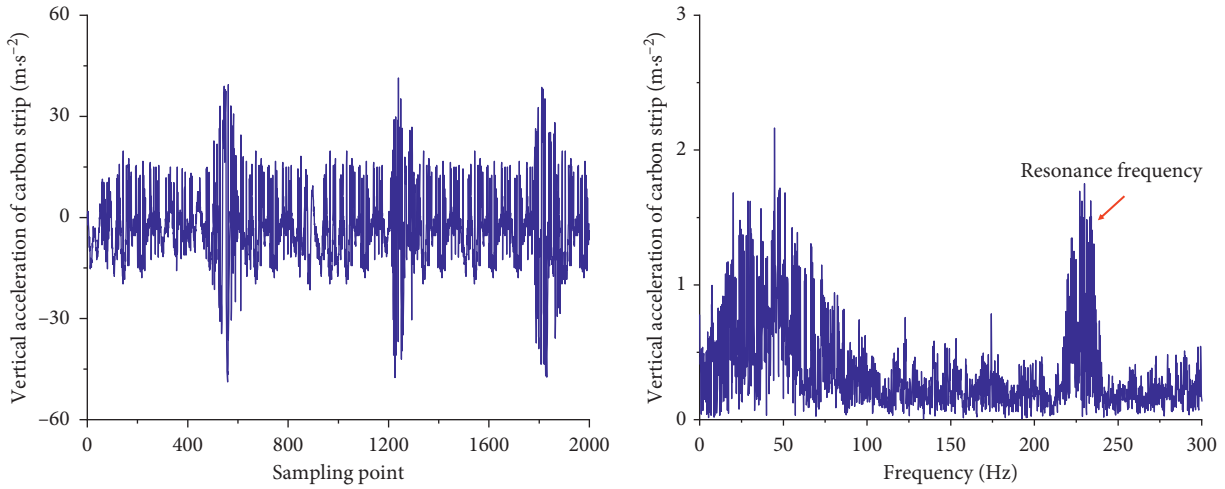

(a) (b)

Figure 13: Time-domain diagram and spectrum of vertical acceleration of carbon strip.

by that at approximately 230 Hz. Based on the results of the modal analysis in Section 3, it can be concluded that the carbon strip and catenary are in resonance during operation, and the resonance frequency is the third modal frequency of the carbon strip. This phenomenon has an instantaneous impact on the contact force: it results in the offline phenomenon between the carbon strip and catenary, which aggravates the arc and mechanical degrees of wear of the carbon strip [27]. According to Figure 13, the vertical acceleration of the carbon strip changes periodically along the rigid catenary span and reaches maxima in the range of 0–100 Hz and at approximately 230 Hz, which is consistent with the results in Figure 12. Hence, the wear of the carbon strip is intensified owing to the resonance in the actual operation. Because the depth of the irregular wear profile and high-frequency vibration are correlated, optimizing the vibration characteristics of the carbon strip is crucial for mitigating irregular wear.

5. Optimization Design

5.1. Optimization Design Theory. Based on the results in Section 4, avoiding the resonance frequency of the carbon strip and catenary and reducing its response amplitude are effective measures for mitigating irregular wear. Therefore, the modal frequency of each mode and the response peak of the vertical vibration are two important indexes for evaluating the optimization effect of carbon strip structures. By considering the vertical and transversal vibration characteristics of carbon strips, the optimization schemes in [28–30] included adding unequal damping (vertical optimization) to the carbon strip structure and changing the cross section of the carbon strip (transversal optimization), respectively. The corresponding mathematical model can be expressed as follows:

$$\begin{cases} \min: q_1(\eta_c, s_c), \\ q_2(\eta_c, s_c) < \omega_c, \\ \dfrac{\Delta m}{m_0}(\eta_c, s_c) < A, \\ \dfrac{abs(\Delta\omega_i)}{\omega_i}(\eta_c, s_c) < B, \end{cases} \tag{16}$$

where q_1 and q_2 are the object functions of the peak vertical vibration acceleration and each modal frequency after the optimization, respectively; η_c and s_c represent the damping parameters and carbon strip cross section as design variables, respectively; ω_c is the mode frequency of each mode before the optimization; and (Δ_m/m_0) and $abs((\Delta\omega_i)/\omega_i)$ are the upper limit of the relative increase in the mass of the carbon strip structure and the relative change in the modal frequency of each order, respectively. The object functions q_1 and q_2 can be written as follows:

$$q_1 = \frac{\left(\sum_{i=1}^{N_c}\left(R_{\max,i}/R_{\max,i}'\right)\right)}{N_c}, \tag{17}$$

$$q_2 = \frac{\sum_{i=1}^{N_c}\left|\omega_{c,i} - \omega_{c,i}'\right|}{N_c}, \tag{18}$$

where $R_{\max,i}'$ and $R_{\max,i}$ are the response peaks of the first-order vibration acceleration before and after the optimization, respectively. The lower q_1 under the constraint conditions is, the better the optimization effect is. Moreover, $\omega_{c,i}'$ and $\omega_{c,i}$ are the modal frequencies before and after the optimization, respectively; the higher q_2 under the constraint conditions is, the better the optimization effect is.

Based on the optimization model and laboratory conditions, the optimization design is divided into different sections of carbon strip and different damping parameters for experimental comparative analysis [31]. According to the wear profile in Figure 11, the deepest part of the wear is the response peak value, so the best effect can be seen by single-input and single-output. The signal excitation and response points are illustrated in Figure 14. The red and black arrows represent the excitation and response points, respectively.

5.2. Optimization Results of Different Damping Parameters. The same experimental principle and environment as in Section 3 were adopted for the modal test. The three schemes were designed according to different damping parameters to compare the corresponding modal parameters [32]. The first scheme represents the original carbon strip structure; in the second scheme, the weight of the original carbon strip aluminum base was changed, and the damping was increased; the weight was 1.2 times that of the first scheme; in the third scheme, the weight of the original carbon strip aluminum base was further changed, and the damping was increased to 1.4 times that of the first scheme. The damping properties of the modes of all three schemes were determined in subsequent modal tests. To compare the experimental results, the same excitation and response points were used, and equal carbon strips with trapezoidal cross sections were used. The modal frequencies and damping ratios of the three schemes are listed in Table 5, and Figure 15 compares the frequency response curves of the three schemes.

As shown in Figure 15(a), the decreases in the response peak in the third, fifth, and sixth modes are particularly pronounced. In the third mode (dashed rectangle), the response peak of scheme 2 is 5 dB higher than that of scheme 1, and the response peak of scheme 3 is 7 dB lower than that of scheme 1. The fifth and sixth modes have the same trend. Thus, scheme 3 is more effective in reducing the response peak than scheme 2. According to Table 5, the modal frequencies of scheme 2 are higher than those of scheme 3 and lower than those of scheme 1. The trend of the damping ratio of the three schemes is opposite to that of the modal frequency. Hence, both schemes can effectively avoid the resonance frequency, while the effect of scheme 3 is better. Moreover, the range of modal frequencies and response peaks in the first mode is short. Owing to the damping vibration isolation mechanism, the bottom modal frequency determines the vibration transfer characteristics and isolation range. As shown in Table 5, scheme 3 has the lowest first modal frequency and highest damping ratio. Thus, the scheme has a wider vibration isolation range and a more effective vibration isolation effect. Furthermore, Figure 15(c) shows that the frequency response peak in the third mode is low, whereas the optimization effect is evident. This confirms the effectiveness of the optimization schemes with different excitation responses.

5.3. Optimization Results of Different Cross Sections. In addition to the damping parameters, the cross-sectional shape of the carbon strip may affect its modal response. Therefore, carbon strips with two different cross-sectional shapes were investigated; the optimal damping scheme in Section 5.2 was adopted to analyze the influence of the cross-sectional shape on the modes of each order. Figure 16 presents the trapezoidal (TC)

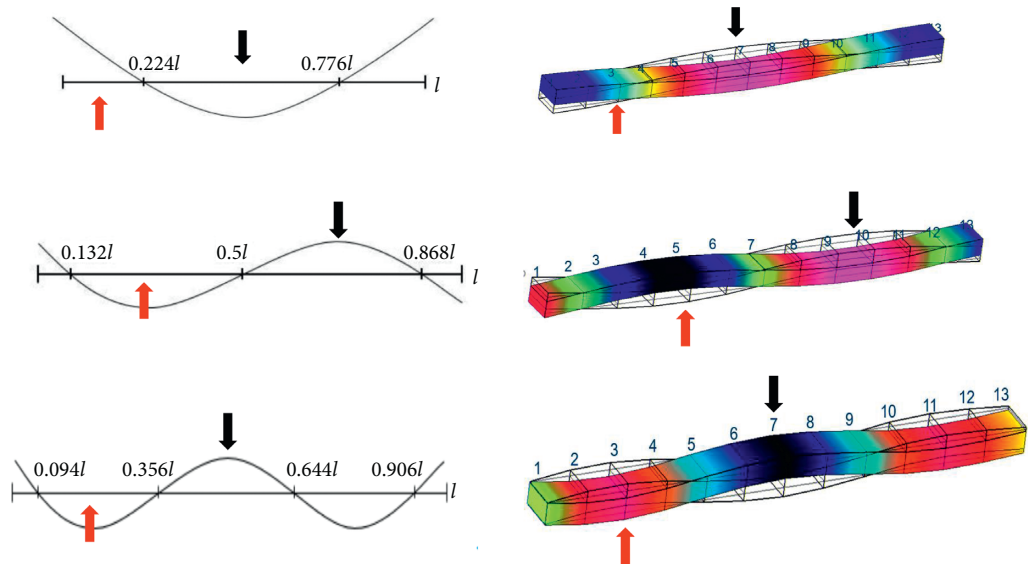

Figure 14: Location distribution of excitation and response points.

Table 5: Modal frequencies and damping ratios of trapezoidal carbon strips with different damping parameters.

Mode	Scheme 1		Scheme 2		Scheme 3	
	Frequency (Hz)	Damping ratio	Frequency (Hz)	Damping ratio	Frequency (Hz)	Damping ratio
First	63.4	1.466	56.4	1.810	51.4	2.155
Second	141.9	0.523	122.6	1.233	112.9	1.654
Third	242.6	0.862	212.8	1.680	194.2	1.379
Fourth	396.3	1.652	349.7	1.785	320.9	2.511
Fifth	595.3	1.471	514.0	1.602	482.9	1.661
Sixth	827.4	0.580	714.5	1.225	661.8	1.559

and rectangular (RC) cross sections of two carbon strips. In addition, Figure 17 compares the frequency response curves of the rectangular and trapezoidal cross sections before the optimization (scheme 1) and the peak decrease of the modal response of each mode after the optimization.

The original frequency response functions of the trapezoidal and rectangular cross sections are illustrated in Figure 17(a). Based on the conclusion in Section 5.2, only one signal input/output scheme was analyzed; the excitation originated at position 2; and the signal was recorded at position 7. The frequency responses of the rectangular and trapezoidal cross sections are not significantly different in the first three modes. In addition, the response functions fluctuate over 400 Hz. According to the experimental results, with the optimization of the damping parameter for each mode frequency, the peak response attenuation of the carbon strip with rectangular cross section is generally greater than that of the carbon strip with the trapezoidal cross section. The excitation/sampling scheme 2 shows the greatest differences in the performance. Accordingly, carbon strips with rectangular cross sections are better in reducing the peak response of each order frequency and thereby mitigating irregular wear of carbon strips than those with trapezoidal cross sections.

5.4. Results and Evaluation. According to the results in Sections 5.2 and 5.3, different damping parameters and cross sections have different optimization effects. Scheme 3 is more effective than scheme 2 in reducing the modal frequency and response peak of each mode. The declivity of the carbon strip with rectangular cross section is steeper than that with a trapezoidal cross section after the optimization. Table 6 presents the calculation results of the model parameters of the two optimization schemes for different cross sections; the q_1 index of scheme 3 is smaller and the q_2 index is greater than that of scheme 2, and the rectangular cross section has a smaller q_1 and greater q_2 index than the trapezoidal cross section. These results are consistent with the previously presented optimization results and thereby confirm the accuracy of the optimization model.

6. Conclusions

In this paper, a numerical model for analyzing the irregular wear of carbon strips based on the vibration mode is proposed; the model is based on a rigid catenary and pantograph with a single degree of freedom. First, the vibration characteristics of the carbon strip were analyzed with the numerical model and then validated in experiments. The modal analysis results show that the mode shapes are significantly correlated with the irregular wear profile of the carbon strip; in addition, the wear profile of the two-groove carbon strip is consistent with the third mode shape, which was confirmed with the numerical model. On this basis, the carbon strip structure and cross section were optimized, and the

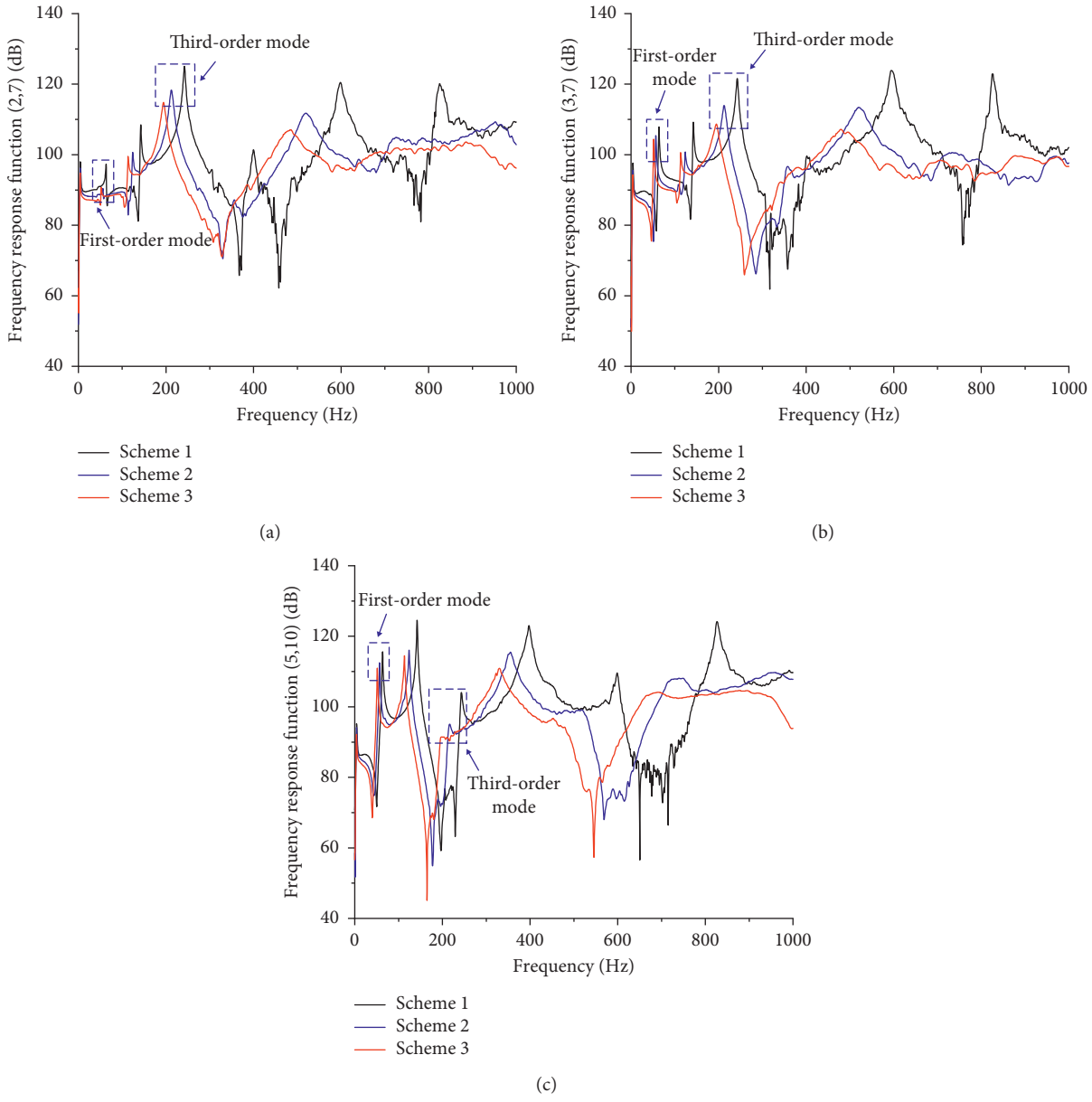

Figure 15: Frequency response functions at different damping parameters in trapezoidal cross section: excitation response at points (a) (2, 7), (b) (3, 7), and (c) (5, 10).

Figure 16: Trapezoidal and rectangular cross sections of carbon strips.

mechanism of irregular wear on the carbon strip was discussed based on the modal analysis. The main conclusions are as follows:

(1) The vertical vibration of the carbon strip is the main factor of irregular wear with two and three grooves, and transverse vibration causes partial wear and edge drops on the carbon strip.

(2) The abnormal-wear profiles of the two and three grooves in the carbon strip are consistent with the third and fifth mode shapes in the modal test. When the

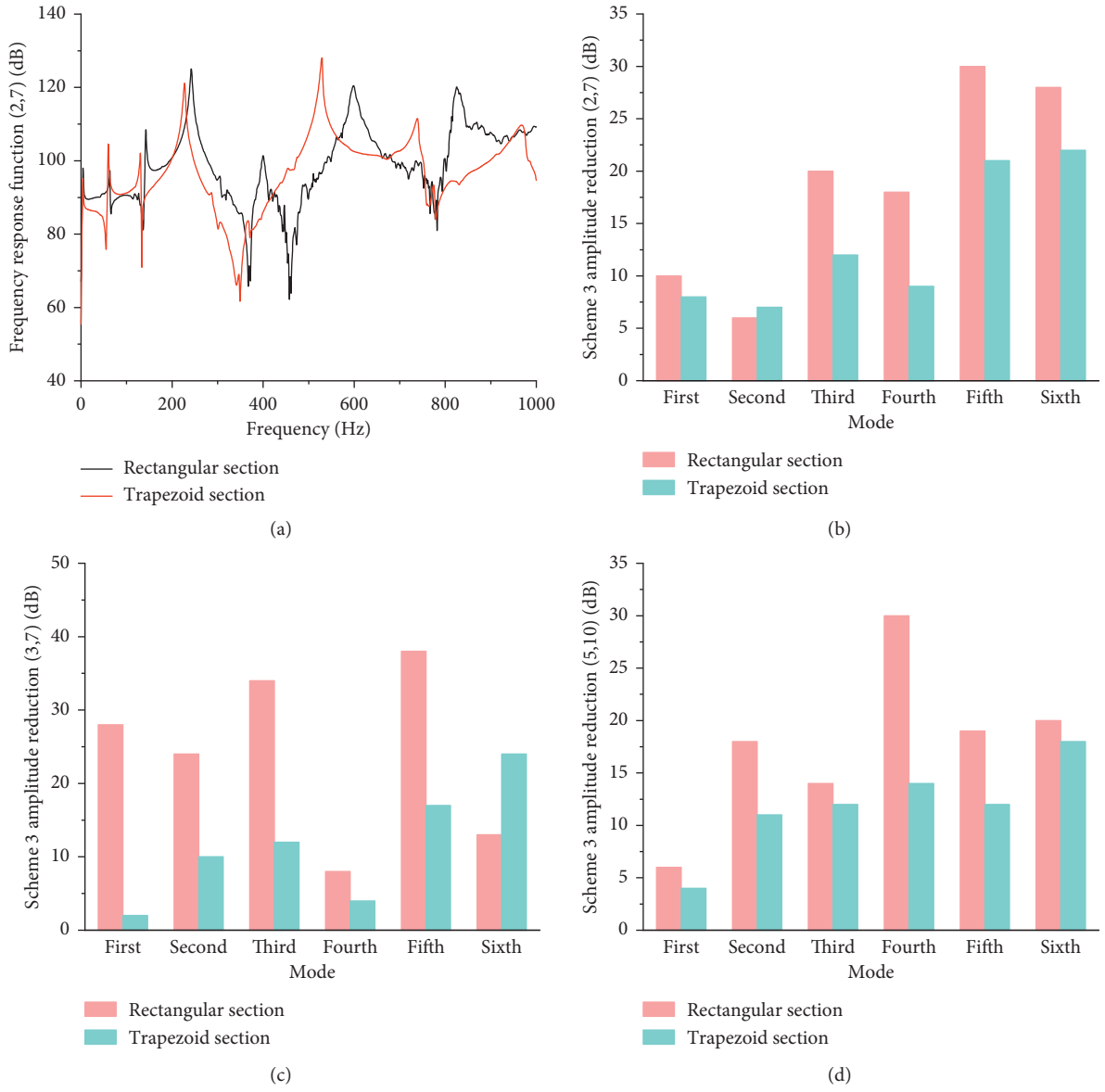

Figure 17: Comparison of frequency response curves and amplitude reductions of rectangular and trapezoidal cross sections before and after optimization.

Table 6: Parameter calculation of the optimization model for schemes 2 and 3 for different cross sections.

Model parameters (incentive response point)	Trapezoidal cross section		Rectangular cross section	
	Scheme 2	Scheme 3	Scheme 2	Scheme 3
q_1 (2, 7)	0.901	0.887	0.889	0.868
q_2 (2, 7)	49.483	73.800	56.352	81.625
q_1 (3, 7)	0.926	0.899	0.885	0.736
q_2 (3, 7)	48.384	72.951	56.241	82.176
q_1 (5, 10)	0.925	0.899	0.886	0.855
q_2 (5, 10)	49.862	74.870	57.368	81.979

pantograph runs at 60 km/h, the carbon strip resonates with the catenary at approximately 230 Hz. Thus, the modal frequency of approximately 230 Hz is the main vibration frequency that causes the two grooves.

(3) The optimization schemes can avoid the harmful vibration frequency and reduce the response peaks. Scheme 3 has the most significant reduction effect on the modal frequency and response peak,

and the decreased response peak of the rectangular cross-section results in a better performance than that of the trapezoidal cross section of the carbon strip.

Data Availability

The raw/processed data required to reproduce these findings cannot be shared at this time as the data also form part of an ongoing study.

Conflicts of Interest

The authors declare that there are no conflicts of interest regarding the publication of this paper.

Acknowledgments

This work was supported by the Natural National Science Foundation of China (NSFC) (no. U1834201).

References

[1] J. A. Bares, N. Argibay, N. Mauntler et al., "High current density copper-on-copper sliding electrical contacts at low sliding velocities," *Wear*, vol. 267, no. 1–4, pp. 417–424, 2009.

[2] J. P. Tu, W. X. Qi, Y. Z. Yang et al., "Effect of aging treatment on the electrical sliding wear behavior of Cu-Cr-Zr alloy," *Wear*, vol. 249, no. 10-11, pp. 1021–1027, 2001.

[3] Y. Kubota, S. Nagasaka, T. Miyauchi, C. Yamashita, and H. Kakishima, "Sliding wear behavior of copper alloy impregnated C/C composites under an electrical current," *Wear*, vol. 302, no. 1-2, pp. 1492–1498, 2013.

[4] X.-Z. Lin, M.-H. Zhu, J.-L. Mo, G.-X. Chen, X.-S. Jin, and Z.-R. Zhou, "Tribological and electric-arc behaviors of carbon/copper pair during sliding friction process with electric current applied," *Transactions of Nonferrous Metals Society of China*, vol. 21, no. 2, pp. 292–299, 2011.

[5] R. Tyagi, D. Xiong, and J. Li, "Effect of load and sliding speed on friction and wear behavior of silver/h-BN containing Ni-base P/M composites," *Wear*, vol. 270, no. 7-8, pp. 423–430, 2011.

[6] I. Yasar, A. Canakci, and F. Arslan, "The effect of brush spring pressure on the wear behaviour of copper-graphite brushes with electrical current," *Tribology International*, vol. 40, no. 9, pp. 1381–1386, 2007.

[7] G. X. Chen, H. J. Yang, W. H. Zhang, X. Wang, S. D. Zhang, and Z. R. Zhou, "Experimental study on arc ablation occurring in a contact strip rubbing against a contact wire with electrical current," *Tribology International*, vol. 61, pp. 88–94, 2013.

[8] T. Ding, G.-X. Chen, Y.-M. Li, Q.-D. He, and W.-J. Xuan, "Friction and wear behavior of pantograph strips sliding against copper contact wire with electric current," *AASRI Procedia*, vol. 2, pp. 288–292, 2012.

[9] H. Yang, G. Chen, S. Zhang, and W. Zhang, "Effect of the vibration on friction and wear behavior between the carbon strip and copper contact wire pair," *Proceedings of the Institution of Mechanical Engineers, Part J: Journal of Engineering Tribology*, vol. 226, no. 8, pp. 722–728, 2012.

[10] G. Mei, "Tribological performance of rigid overhead lines against pantograph sliders under DC passage," *Tribology International*, vol. 151, p. 106538, 2020.

[11] Y. Y. Zhang, Y. Z. Zhang, S. M. Du, C. F. Song, Z. H. Yang, and B. Shangguan, "Tribological properties of pure carbon strip affected by dynamic contact force during current-carrying sliding," *Tribology International*, vol. 123, pp. 256–265, 2018.

[12] G. Bucca and A. Collina, "Electromechanical interaction between carbon-based pantograph strip and copper contact wire: a heuristic wear model," *Tribology International*, vol. 92, pp. 47–56, 2015.

[13] X. K. Wei, H. F. Meng, J. H. He, L. M. Jia, and Z. G. Li, "Wear analysis and prediction of rigid catenary contact wire and pantograph strip for railway system," *Wear*, vol. 442-443, p. 203118, 2020.

[14] N. Zhou and W. H. Zhang, "Analysis of dynamic pantograph-catenary interaction based on elastic pantograph model," *Journal of Rail Way Society*, vol. 31, no. 6, pp. 26–32, 2009.

[15] Y. Shi, J. H. Lin, Z. Zhuang, and Z. C. Liu, "Fault diagnosis for pantograph cracks based on time-frequency decomposition and sample entropy of vibration signals," *Journal of Vibration and Shock*, vol. 38, no. 8, pp. 180–187, 2019.

[16] M. Simarro, S. Postigo, J. A. Cabrera, and J. J. Castillo, "A procedure for validating rigid catenary models using evolutionary techniques," *Computers & Structures*, vol. 228, 2020.

[17] N. Zhou and W. H. Zhang, "Dynamical performance simulation of the pantograph-catenary coupled system based on direct integration method," *China Railway Science*, vol. 29, no. 6, pp. 71–76, 2008.

[18] P. Mercorelli, M. Rode, and P. Terwiesch, "A wavelet packet algorithm for online detection of pantograph vibrations," *IFAC Proceedings Volumes*, vol. 33, no. 9, pp. 235–240, 2000.

[19] A. Facchinetti and S. Bruni, "Hardware-in-the-loop hybrid simulation of pantograph-catenary interaction," *Journal of Sound and Vibration*, vol. 331, no. 12, pp. 2783–2797, 2012.

[20] Y. Xu, R. F. Wang, and J. T. Li, "Study on the relationship between pantograph contact pressure and carbon strip wear of urban rail transit vehicles," *Railway Locomotive & Car*, vol. 39, no. 3, pp. 67–71, 2019.

[21] Y. Hu, B. J. Dong, H. Huang, G. X. Chen, G. N. Wu, and G. Q. Gao, "Friction and wear behavior of carbon strip/contact wire," *Journal of Transportation Engineering*, vol. 16, no. 2, pp. 56–63, 2016.

[22] Y. Hu, B. J. Dong, H. Huang et al., "Experimental study on the temperature rise of a carbon strip and its influence on the wear performances of the carbon strip," *Tribology International*, vol. 35, no. 6, pp. 677–683, 2015.

[23] J. Zhang, K. Maes, G. De Roeck, E. Reynders, C. Papadimitriou, and G. Lombaert, "Optimal sensor placement for multi-setup modal analysis of structures," *Journal of Sound and Vibration*, vol. 401, pp. 214–232, 2017.

[24] R. S. Bayma, Y. Zhu, and Z.-Q. Lang, "The analysis of nonlinear systems in the frequency domain using nonlinear output frequency response functions," *Automatica*, vol. 94, pp. 452–457, 2018.

[25] A. B. Wang, Z. Q. Wang, P. Zhang, and Y. Y. Zhang, "The mechanism and control of the generation and development of wave wear of rail," *Material Development and Application*, vol. 31, no. 6, pp. 6–15, 2014.

[26] Y. Hu, G. X. Chen, S. D. Zhang et al., "Comparative investigation into the friction and wear behaviours of a Cu-Ag contact wire/carbon strip and a pure copper contact wire/carbon strip at high speeds," *Wear*, vol. 376-377, pp. 1552–1557, 2017.

[27] P. Wang, H. Zhang, J. Yin, X. Xiong, and C. Deng, "Effects of fibre orientation on wear behavior of copper mesh modified-

carbon/carbon composite under electric current," *Tribology International*, vol. 116, pp. 310–319, 2017.

[28] M. E. Mansori, D. Paulmier, J. Ginsztler, and M. Horvath, "Lubrication mechanisms of a sliding contact by simultaneous action of electric current and magnetic field," *Wear*, vol. 225-229, no. 4, pp. 1011–1016, 1999.

[29] X. Li, D. Zhou, L. Jia, and M. Yang, "Effects of yaw angle on the unsteady aerodynamic performance of the pantograph of a high-speed train under crosswind," *Journal of Wind Engineering and Industrial Aerodynamics*, vol. 182, pp. 49–60, 2018.

[30] N. Zhou and W. Zhang, "Investigation on dynamic performance and parameter optimization design of pantograph and catenary system," *Finite Elements in Analysis and Design*, vol. 47, no. 3, pp. 288–295, 2011.

[31] Y. H. Cho, K. Lee, Y. Park, B. Kang, and K.-n. Kim, "Influence of contact wire pre-sag on the dynamics of pantograph-railway catenary," *International Journal of Mechanical Sciences*, vol. 52, no. 11, pp. 1471–1490, 2010.

[32] C. Xue, X. X. Xu, Z. F. Su et al., "Experiment of identifying semi-active particle damping loss factor based on steady-state energy flow method," *Journal of Aerospace Power*, vol. 35, no. 1, pp. 60–65, 2020.